UNIVERSITY of the
WESTERN CAPE

Visible and IR photoluminescence of c-FeSi@a–Si core–shell nano-fibres produced by vapour transport

Sibongiseni Thabethe, EllaLinganiso, DavidMotaung, MateteG.Mashapa, StevenNkosi, Christopher J. Arendse and Bonex W. Mwakikung

Abstract

The procedures for the synthesis of amorphous ε-FeSi/Si core–shell nanofibres by vapour transport in a CVD configuration are reported. Crystallite studies by the Williamson-Hall method show the sizes to be typically about 8.0 nm which agrees with TEM value of 7.9 nm fibre diameter with a compressive strain of about 0.04. Features in the photoluminescence of these FeSi core–shells in both visible and IR are at 410 nm, 1062 nm, 1414 nm and 1772 nm and absorption feature at 1000 cm^{-1} from FTIR are explained from density functional theory (DFT) ab initio calculations. PL confirms the intra-band transition whereas FTIR agrees perfectly with the band-to-band transition whose band gap energy is 0.13 eV for FeSi. FTIR also unveils inter-band transition which DFT calculation could not predict. Raman spectroscopy data confirm FeSi and nano-Si presence.

1. Introduction

One-dimensional (1-D) inorganic nanowire materials have enjoyed prominent attention in the research community in the past decade because they can be rationally and controllably synthesized and have found many promising applications in electronics, photonics, spintro- nics, sensing, photovoltaics and thermoelectrics. These nanostructures exhibit fascinating physical and chemical properties distinct from those of bulk or thin film materials [1–4]. Experimental conditions such as reaction time and temperature play an important role in the morphology of the reaction products. Unique morphologies of FeSi nanostructures such as nanocombs [4], nanoflowers [5] and hyper- branched nanowires [5] have been reported. For the synthesis of 1-D nanowires, metal-catalyzed chemical vapour deposition (CVD) has proven to be one of the most successful growth methods as it offers convenience compared to wet chemical methods. CVD here works well since the object was to obtain the alloy of Fe and Si. In wet chemistry methods, it is difficult to find solvent that are free from oxygen and other impurities. The temperatures used here may be similar to those used in other reports; however, synthesis of FeSi from the Fe containing $FeCl_3$ precursor and the heated Si substrate is new. However, metal contaminations are often detrimental to their applications. Growth by a spontaneous chemical vapour transport method without the use of a catalyst is favoured if

the method proves to be a viable alternative [5,6]. Silicides form an important group of transition metal compounds with interesting physical properties. The majority of silicides turn out to be metallic, some of them, including the B20 cubic phase of iron monosilicide (FeSi) have been found to exhibit semi- conducting properties ($E_g = 0.1$ eV) below room temperature and a metal to insulator transition (MIT) around 300 K [7–11]. Its transition temperature makes this material a good candidate in the field of gas sensing as well as in thermochromism where the material could keep homes warm in winter and cool in hot summer when coated on window glass as is the case for vanadium dioxide (VO_2) [12–15]. The disadvantage with VO_2 is that its MIT is at 340 K [16–18] which is 40 1C above room temperature, and it requires doping with metals such as W, Cr and Nb for its MIT to shift to room temperature. The doping of VO_2 comes at the expense of its switching contrast. FeSi has its MIT already at room temperature, naturally, and the relative abundance of Fe and Si are the major advantages of shifting research attention to FeSi.

In this paper, we report on the noodle-like nanofibres of FeSi obtained by vapour transport in a chemical vapour deposition (CVD) configuration. In addition we report on the luminescent properties of FeSi nanofibres which appear in the IR through blue to UV regions and IR absorption properties which reveal other transitions in FeSi that a standard photoluminescence spectrometer could not give.

2. Experimental

$FeCl_3$ powder (97% Purity) and Si (1 1 1) wafers were purchased from Sigma-Aldrich and were used as received. The other 3% of the $FeCl_3$ powder (97% Purity) is documented in the suppliers (Sigma- Aldrich) which are trace elements of Na, K and Ca. For the synthesis of FeSi nanostructure, Fe source precursor $FeCl_3$ was placed at the centre of the horizontal quartz tube furnace in quartz boat. Si(1 1 1) substrates were placed 1–2 cm away from the Fe source. The temperature of the furnace was adjusted from room temperature to 1100 1C. N_2 gas was used a carrier gas to transport the precursor vapours from the $FeCl_3$ to the silicon substrates and the reaction was performed for 1 h 40 min. After cooling down to room temperature in air, the Si substrates were taken out for further analysis.

The morphology of the products formed on the silicon sub- strates was examined using focused ion beam (FIB) field emission scanning electron microscopy (FE-SEM) (Auriga Cobra FIB FESEM). The crystallinity of the nanostructures was analyzed using high resolution transmission electron microscopy (HR-TEM) (JEOL-JEM 2100). Nanostructures removed from the Si substrates were dis- persed in ethanol, and TEM copper grids were dipped into the solution and analysed. The structural properties were examined using Panalytical X'pert PRO PW 3040/60 X-ray diffractometer (XRD) with a Cu $K\alpha$ (λ¼ 0.154 nm) monochromated radiation source.

The photoluminescence (PL) properties of the nanostructures were investigated using a spectro-fluorometer (Jobin Yvon Nano- log FL3-22) at room temperature. The emission was detected with Jobin-Yvon PMT detector. In order to explain the new features in the PL

spectra of these FeSi nano-structures, band structure and density of states (DOS) calculations were undertaken.

We carried out density functional theory simulations using the generalized gradient approximation (GGA) and the local density approximation (LDA) [19] for the exchange and correlation func- tional, as implemented in the CASTEP code [20]. The interaction between the ionic cores and the valence electrons is described using ultra soft pseudo potential of Vanderbilt [21]. The Brillouin zone of FeSi is sampled using the scheme of Monkhorst and Pack [22] This kind of k-point sampling method gives a good convergence to the total energy calculations. A kinetic energy cut-off of 300 eV was used for the plane wave expansion of the wavefunctions. The positions of all atoms in the defective nanotubes were relaxed using the conjugate gradient algorithm with a tolerance of 2×10^{-5} eV for maximal change in total energy. Calculations converged when the residual forces were less than 0.05 eV/Å. The electronic states were occupied in accordance with the Fermi distribution function using a Fermi smearing parameter of $k_B T \frac{1}{4}$ 0.20 eV.

3. Results and discussion
3.1 Morphology and structural properties of FeSi nanofibres
Fig. 1 shows a scanning electron microscopy (SEM) image of the bundles of interwoven fibrous nanostructures. The diameter of a single strand ranged from 20 nm to 100 nm with a single strand composed of 7–8 single FeSi fibres. The mingling of the FeSi nanofibres could be a result of an indeterminate growth direction and the presence of many growth nuclei at the surface of the Si substrate. The other reason for non-directionality is that the nanofibres have a diameter of about 8 nm. This is too thin compared to the roughness of the Si surface which of the order of 100's of nm. This roughness influences the meandering mor- phology of the subsequent FeSi/Si core–shell nanofibres. Because no catalyst was used, Si is inevitably one of the candidates in the fibres. Previous synthesis of FeSi without catalysis reports presence of amorphous SiO_2 [5]. One notes that the nanofibres in Fig. 1 appear outstandingly bright against the substrate back- ground. This over-brightness could be due to electron charging effect owing to the loose attachments of the fibres to the grounded substrate. However, if the secondary electron detector also detected photons as a result of the electron–FeSi phonon interaction and if the fibres are well attached to the ground, the over-brightness could be due to cathodoluminescence (CL) from the FeSi nano-fibres. CL spectra could not be performed due to the limitations of the instrument.

A high resolution transmission electron microscopy (HRTEM) micrograph is shown in Fig. 2. The nanostructures appeared to have core–shell structures and are semi-crystalline indicating that the nanostructures composed of an amorphous network and crystalline region. The core is dense and crystalline, whereas the shell is amorphous. Szczech et al. [1] found that when they performed surface characterization of the individual FeSi nano-wires with X-ray Photoelectron Spectroscopy (XPS), that the sur- face oxide layer formed on the nanowires was in fact not Fe_2O_3, but SiO_2, which was consistent with the fact that

3

FeSi will develop a thin silicon oxide layer during exposure to air. In our case, the amorphous shell is in fact Si as shown in the localised energy dispersive spectroscopy (EDS) performed at the core and around the shell in Fig. 2(c) and (d). The few peaks of Fe in the local EDS for the shell could be small contributions from core.

X-ray diffraction was performed on the deposited nanostruc- tures. All the observed diffraction peaks are indexed to FeSi (Fig. 3), which has a cubic structure with a lattice constant of 4.496 Å (space group P2₁3, Pearson symbol cP8, structure type FeSi, $Z \frac{1}{4} 4$, JCPDS PDF 76-1748, 88-1298 and 89-2677). In order to estimate the crystallite size, the Debye-Scherrer [23] method is employed, which states that the peak width B(2θ) is inversely proportional to the crystal size (L) i.e.

$$B = \frac{0.94\lambda}{L \cos\theta} \tag{1}$$

where λ is the X-ray wavelength and θ is the Bragg angle for the individual peaks starting from 2θ = 281 to 2θ= 611, the crystallite sizes were found to range from 13.9 nm to 131.1 nm (Table 1). In addition to the Debye-Scherrer method, a second method for estimating the crystal size was used, namely the Williamson–Hall 24]. This method accounts for both strain and crystallite size of the material i.e.

$$B = C\varepsilon \tan\theta + \frac{0.94\lambda}{L \cos\theta} \tag{2}$$

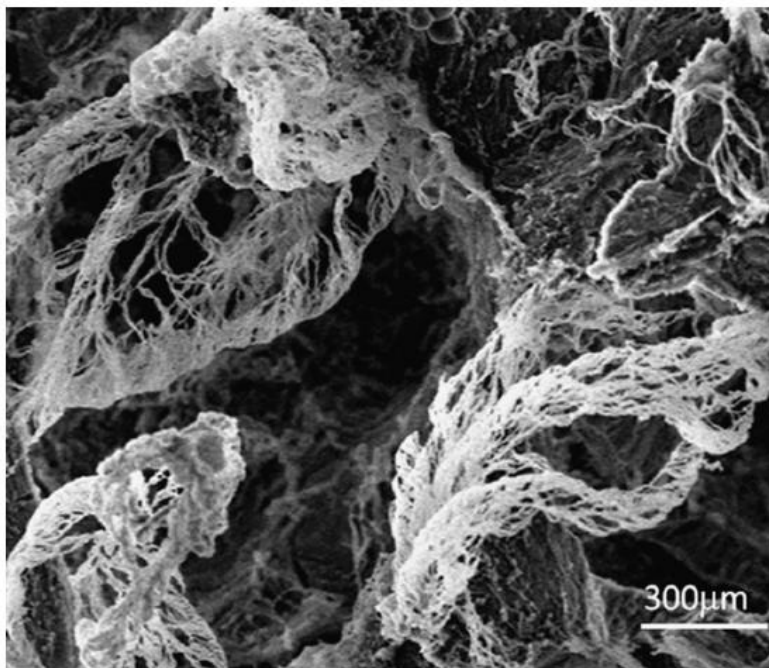where (Cε) is the strain component.

4

Fig. 1. Representative SEM image of the interwoven FeSi fibres. Note that the fibres are outstandingly bright against the background. This could be due to electron charging effects as well cathodoluminescence.
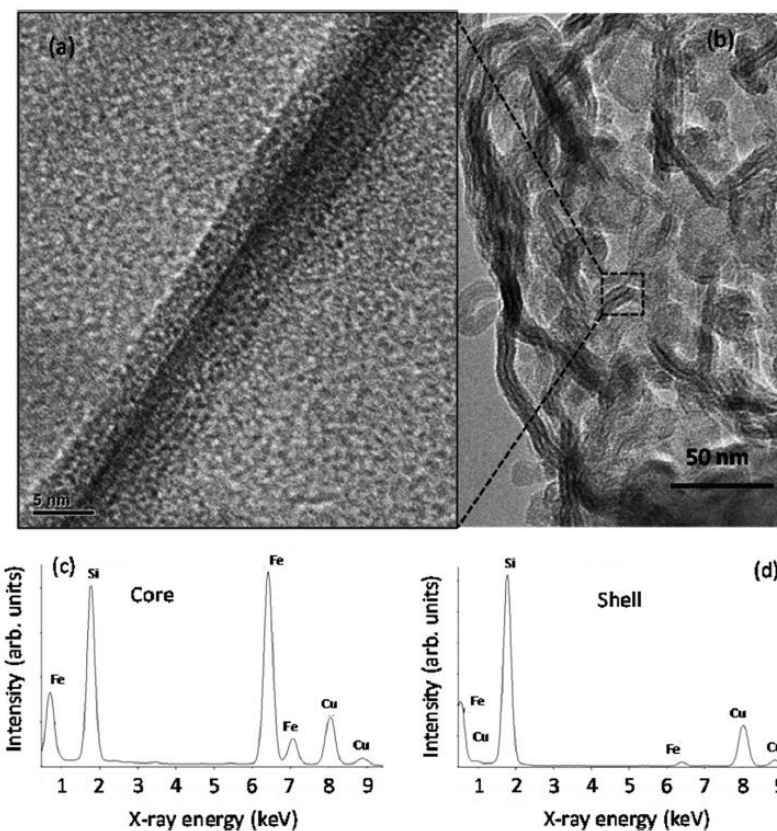

Fig. 2. (a) TEM image of a single core–shell FeSi nanofiber; a dense and crystalline FeSi core surrounded by Si-rich amorphous shell and (b) TEM image of the tangled FeSi nanofibers. (c) local EDS of the core and (d) local EDS of the shell.
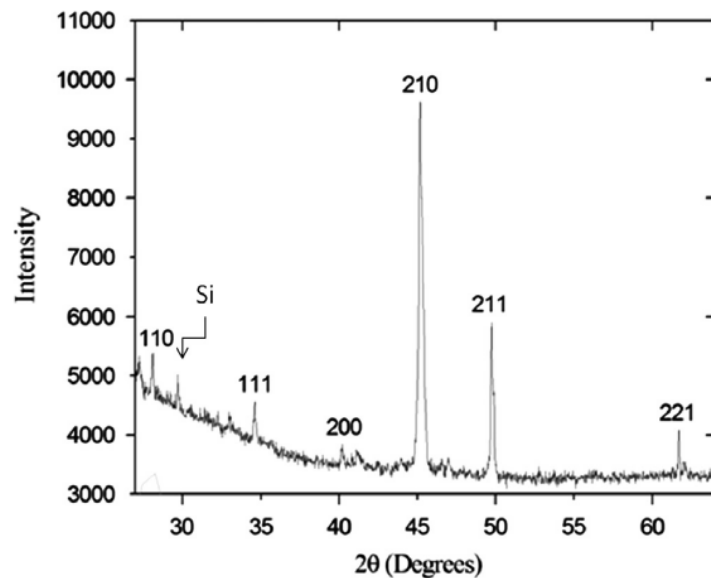
5

Fig. 3. XRD of the FeSi nanofibers.

This calculated crystallite size differs significantly from the Debye–Scherrer crystallite size as shown in Table 1, but the Williamson–Hall calculation agrees with the HRTEM measurements. For all the planes the estimated crystallite size is 1.93 nm but when only the FeSi main peaks are considered, the crystallite diameter by the Williamson-Hall plot, is 7.75 nm compared to HRTEM measurement of about 8.00 nm. The Williamson–Hall provided a more accurate estimation of the crystallite sizes, which agrees with our TEM results, thus proving to be a more reliable method.

Fig. 4 shows that the 110 plane is an outlier and does not follow a pattern similar to the other planes. The observed 110 plane might be resulting from contributions from the silicon substrates.

3.2. *Photoluminescence of the FeSi/Si core–shell nanofibres*

The $FeSi_2$ phase's photoluminescence properties have been studied and it has been reported that the material, with a band gap of 0.8 eV, emits at a wavelength of 1.54 μm (0.81 eV) [25–31]. To the best of our knowledge photoluminescence properties of the FeSi have never been reported. Therefore, in this study we report for the first time on the photoluminescence properties of FeSi. By using the excitation energy of 325 nm (3.8 eV), we observe an emission peak around 410 nm (3.02 eV), 1062 nm (1.16 eV), 1414 nm (0.88 eV) and 1717 nm (0.70 eV). There is a strong PL peak between 600 nm and 700 nm. This peak may be as a result of (1) quantum confinement due to the typical crystallite size of about 8 nm of the FeSi core as well as the thinner than 5 nm Si shell and (2) intra-band transitions due to impurity and vacancy defect states in the FeSi structure.

6

On the nano-Si shell, it is known that bulk Si with a band gap of 1.1 eV emits at a wavelength of 1100 nm in conformity with band-to-band transition in Si. Nano-Si has been observed to show a blue shift.

Table 1
Results from Debye–Sherrer model and the Williamson–Hall plot for crystallite sizes and strain in the nano-fibres.

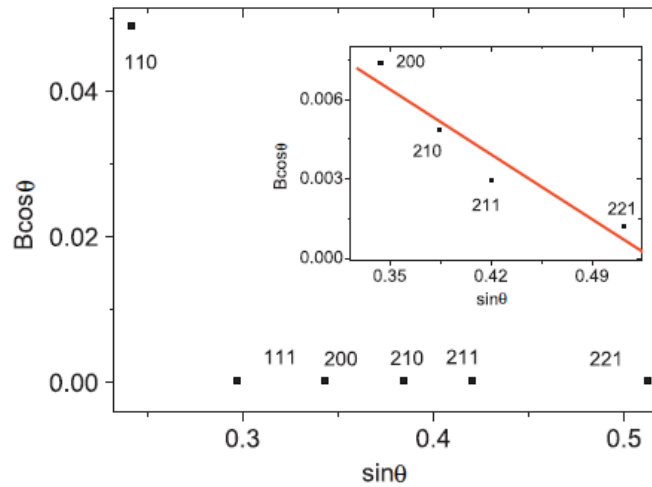| 2θ (Degrees)	Miller planes	Debye–Scherrer (L) (nm)	Williamson–Hall (L) (nm)			
			L, ε values when all peaks are considered		L,ε values when (1 1 0) peaks is excluded	
28	110	83.6				
34.5	111	65.1	L	ε	L	ε
40	200	48.9	1.93	−0.17	7.75	−0.04
45	210	68.1				
49.6	211	13.9				
61.9	221	131.1				

Fig. 4. Williamson–Hall plot.

However the blueshift from 1100 nm to between 600 nm and 700 nm was calculated to be too big for a crystallite size of 5 nm. For instance, from Efros and Efros [32], the change of energy of the emitted photons due to strong, moderate and weak quantum confinement are respectively given as

$$\Delta E = \frac{h^2\pi^2}{2\mu^* R^2} \quad \text{(strong confinement)} \tag{3}$$

$$\Delta E = \frac{h^2\pi^2}{2MR^2} \quad \text{(weak confinement)} \tag{4}$$

$$\Delta E = \frac{h^2\pi^2}{2m_e^* R^2} \quad \text{(verysmall nanoclusters)}$$

$$\Delta E = \frac{h^2\pi^2}{\mu^* R^2} - \frac{1.786e^2}{\in_r R} + 0.284\frac{13.606\, m_0}{\in_r^2(1/m_e^* + 1/m_h^*)} \tag{5}$$

7

where μ^n is the reduced mass of the electron–hole pair (exciton) which is usually taken to be $2m_e$ (with m_e being the mass of the electron), R is the crystallite radius, $M = m_e + m_h$, is the relative dielectric constant of the medium and m_0 is the mass of the proton in hydrogenPerforming a simple calculation for the typical nanofibres presented here, one finds that the 1100 nm peak for bulk Si should shift by 0.1 eV (112 nm) for strong quantum confinement and much less than that value for moderate and weak confine- ment. According to quantum confiment theories, the new peak should shift from 1100 nm to 988 nm. The quantum confinement theoretical equations therefore are not able to singly account for the major shift of the 1100 nm peak down to between 600 nm and 700 nm. It is possible therefore that the second reason of intra- band transitions due to defects is an added contribution to this blue shift.

We therefore explain the second contribution using the band structures of FeSi calculated using LDA and GGA. Band structure and electron density of states calculations performed on the FeSi system are presented in Fig. 6. We attribute the energy dispersion curves of $E43$ eV to Si (3p) and -6 eV$0E0-3$ eV to Fe–Si hybridization, those curves of energy in the range -3 eV$4E4+3$ eV to Fe (3d) electrons and those below -6 eV to Si (3s and 3p) electronic states. The Fe and Si labels are clearly marked in Fig. 6(a) and (b). This assignment is in agreement with the previous calculations [33]. The density of states in (b) show that while most of the electrons belong to Fe (3d) close to the Fermi level, a good proportion are in the valence band confirming the Kondo insulator behaviour in FeSi. For clarity, we have labelled the energy levels differently in this paper and these appear in Fig. 6(c). Those bands with predominant Fe 3d are identified by our labels Fe $3d^2$ to Fe $3d^{-2}$ where positive exponent refers to conduction band and negative refers to valence band and those of Si 3s, 3p orbital character are specified by our label Si $3s^6+3p^6$, Si $3s^5+3p^5$, Si $3s^{-6}+3p^{-6}$, and Si $3s^{-5}+3p^{-5}$.
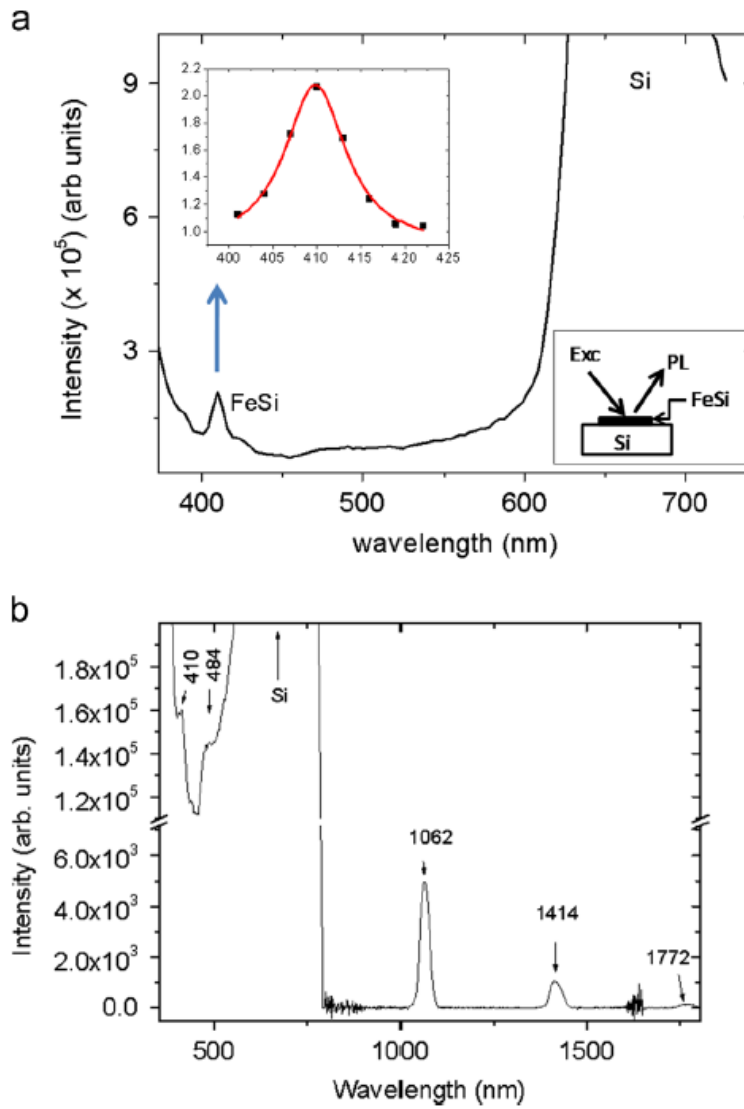
Fig. 5. (a) Visible range photoluminescence spectrum for FeSi nano-fibres excited by a light source of wavelength 325 nm (b) Visible and IR photoluminescence spectra showing the quality of IR spectra compared to the visible range against high background noise.
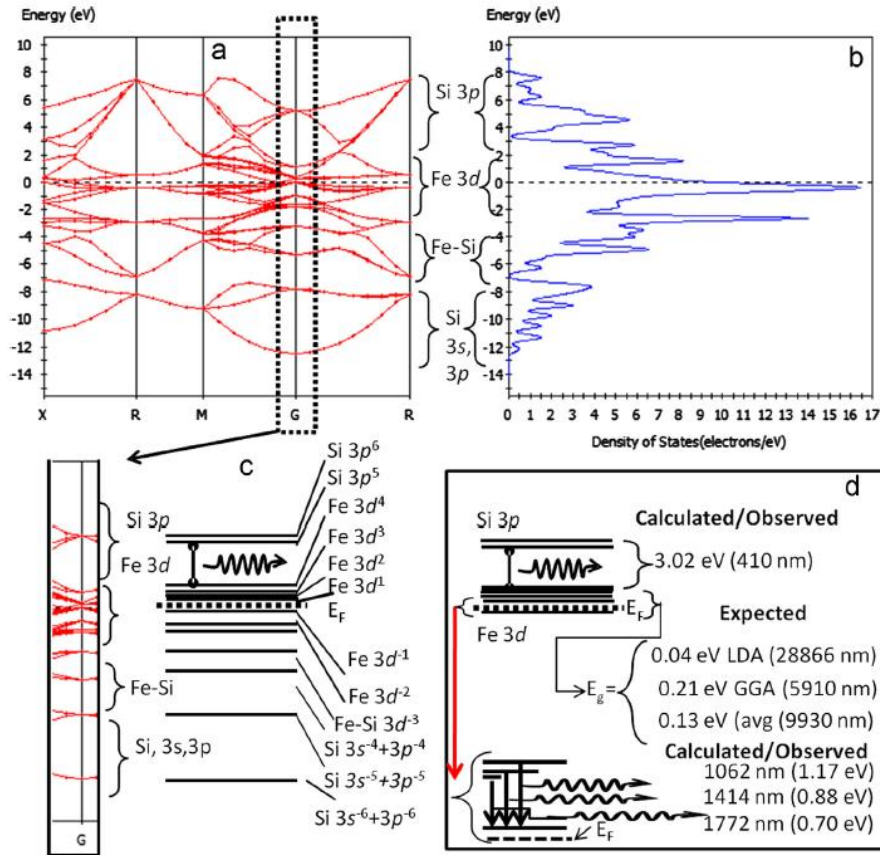
Fig. 6. Assignments of the band structure (a) and DOS (b) to the Si (3p), Fe (3d), Fe–Si hybridization and Si (3s and 3p) electron states. In (c) we consider the gamma, G, symmetry line and introduce our labels for explanation of our PL results in Fig. 5. In (d) the 3.11 eV (410 nm) photon emission is due to the de-excitation from Si (3p) electron states down to the Fe (3d) level.

Table 2
A summary of the transitions in FeSi from DFT and the measured amplitudes from PL with their associated probabilities.

Wavelength, λ(nm)	Transition description	Transition probability (theory)	Amplitude, A_i, (Expt)	Probability (Expt) $A_i/\Sigma_i A$
410 nm (3.02 eV)	$< \text{Si } 3p^5 | \text{Fe } 3d^4 >$	$| < \text{Si } 3p^5 | \text{Fe } 3d^4 > |^2$	1.000	0.125
484 nm (2.56 eV)	$< \text{Si } 3p^5 | \text{Fe } 3d^4 >$	$| < \text{Si } 3p^5 | \text{Fe } 3d^4 > |^2$	0.864	0.108
1062 nm (1.16 eV)	$< \text{Fe } 3d^1 | \text{Fe } 3d^0 | \text{Fe } 3d^{-1} >$	$| < \text{Fe } 3d^1 | \text{Fe } 3d^0 | \text{Fe } 3d^{-1} > |^2$	4.966	0.619
1414 nm (0.88 eV)	$< \text{Fe } 3d^1 | \text{Fe } 3d^0 >$	$| < \text{Fe } 3d^1 | \text{Fe } 3d^0 > |^2$	1.048	0.131
1772 nm (0.70 eV)	$< \text{Fe } 3d^0 | \text{Fe } 3d^{-1} >$	$| < \text{Fe } 3d^0 | \text{Fe } 3d^{-1} > |^2$	0.149	0.019

The lowest grouping of four bands evolves essentially from the Si (3s) states (Si $3s^6+3p^6$, Si $3s^5+3p^5$, Si $3s^{-6}+3p^{-6}$, and Si $3s^{-5}+3p^{-5}$). The bands above these at slightly higher (~ −6 to~−3 eV) energies reflect Si–Fe hybridization effects and their mixed character has been distinguished by labels Si $3s^4+3p^4$, Si $3s^3+3p^3$, Si $3s^{-4}+3p^{-4}$, and Si $3s^{-3}+3p^{-3}$. The Fe 3d bands span the adjoining energy range from about −3 to +3 eV, while hybridized bands with enhanced Si 3p character reappear at higher energies near the top of Fig. 6 with our labels Si $3p^3$ to above Si $3p^6$. In as far as the new photoluminescence feature appearing at 410 nm, we consider the gamma, G, line of symmetry which we have zoomed-in in Fig. 6(c) and our corresponding labels. The gamma point (where $\pi a/\lambda = 0$) being the centre of the Brillouin zone is appropriate when the photon wavelength, λ, of excitation (in this case 325 nm) is much longer than

10

the lattice parameter of the FeSi system ($a\sim$0.47 nm). One of the transitions extracted from the band structure in Fig. 6 to explain the luminescence feature at a wave- length of 410 nm is one of those electrons de-exciting from Si (3p) level down to the Fe (3d) as shown in Fig. 6(d). The other IR features at 1062 nm (1.16 eV), 1414 nm (0.88 eV) and 1772 nm (0.70 eV) are assigned to the transition $\langle$Fe 3d$^1|$Fe 3d$^O|$Fe 3d$^{-1}\rangle$, $\langle$Fe 3d$^1|$Fe 3d$^O\rangle$, and $\langle$Fe 3d$^O|$Fe 3d$^{-1}\rangle$ respectively. The probability that these transitions will occur are defined as the square of each operation respectively written as $|\langle$Fe 3d$^1|$Fe 3d$^O|$Fe 3d$^{-1}\rangle|^2$, $|\langle$Fe 3d$^1|$Fe 3d$^O\rangle|^2$, and $|\langle$Fe 3d$^O|$Fe 3d$^{-1}\rangle|^2$ where the state Fe 3d^O is equivalent to the Fermi level, E_F. These data compared to the amplitudes of the individual peaks in the PL spectra along with all the possible transitions that have been observed by our PL spectro- meter in Table 2. This table shows that the most probable emission from FeSi is the IR emission at 1062 nm which seems equivalent to the YAG emission at 1064 nm.

As already noted about the density of states, the photoluminescence feature at a wavelength of 410 nm, however, seems not to come from the majority of the electrons but from only those that are above the Fermi energy level. More reliable assignment has been accomplished via the band structure in (a); the DOS in (b) only gives an idea of how many electron in a single atom are involved and this can give an indication of the probability of luminescence and hence the magnitude of intensity expected in a typical experimental measurement. In this case one can clearly see why the 410 nm feature has not been reported to date. The features around Fermi level and those just below that level, being contributed from the majority of the electrons, which leads to an emission at around 1540 nm for FeSi$_2$, has been widely reported. In the present case, FeSi shows peaks at 1062 nm, 1414 nm and 1772 nm in this same range. Given large excitation intensities, FeSi can then be employed in UV sources and IR lasers apart from the microwave generators that have so far been reported.

The above intra-band transition assignments have been carried for FeSi for the first time; however similar work has been performed on gold [34].

3.3. Fourier transform infrared spectroscopy and Raman spectroscopy of the FeSi core−shell nanofibres

It must be mentioned that the band to band transitions reveal a band gap of 0.13 eV as an average between 0.21 eV from GGA approximation and 0.04 eV from the LDA approximation. These band to band transitions could not be measured from the PL due to the limitations of the detector as 0.13 eV translates to 12 μm. In order to observe these band to band absorptions, FTIR was performed on the ε-FeSi/Si fibre sample. The FTIR spectrum is given in Fig. 7. Immediately one sees two major absorption peaks at 783 cm^{-1} (0.09 eV) and 1067 cm^{-1} (0.13 eV). The former is a bending vibration of the Fe−Si bond technically referred to as the transverse-optical (TO) phonon whereas the latter can be assigned to the longitudinal optical (LO) FeSi

(stretching mode) phonon. The latter absorption at 0.13 eV agrees perfectly with the band gap energy from our calculations (0.13 eV) as averaged from GGA and LDA as well as in agreement with previous observations as stated in the preceding Introduction section. The FTIR spectrum also reveals other minor inter-band absorptions which could be due to small defects and vacancies in the FeSi lattice.

The Si that forms the shell material is not amorphous. This fact has been confirmed by Raman spectroscopy as shown in Fig. 7(b). Amorphous Si shows a peak at 480 cm^{-1} while crystalline Si has a peak at 520 cm^{-1} [35]. The Raman spectrum from our FeSi/Si fibres show a broad peak between these two extremes centred 490 cm^{-1}. Therefore we can concluded that this peak signifies nano-crystalline Si rather than amorphous Si.

4. Conclusions

We have successfully obtained new FeSi core–shell nanofibres. TEM confirms the shell to be somewhat amorphous while the core is dense and largely crystalline.. XRD does point to the stoichio- metric FeSi with the usual peaks indexed to FeSi which has a cubic structure with a lattice constant of 4.496 Å (space group P2$_1$3, Pearson symbol cP8, structure type FeSi, Z = 4, JCPDS PDF 76–1748, 88–1298 and 89–2677). We have employed both the Debye–Scherrer model and the Williamson–Hall method to determine the crystallite sizes and the strain in the fibres. The Debye model suggests the crystallite size ranges from 13 nm to 130 nm where the Williamson–Hall plot yields a size of about 8 nm and a strain of 0.04. The latter is more agreeable with HRTEM of a single core–shell nano-fibre whose core is 4 nm in diameter and a shell of about 10 nm from edge to edge.

Photoluminescence has revealed new features at a wavelength of about 410 nm, 1062 nm, 1414 nm and 1772 nm. This has been ascribed by ab initio calculation of electronic band structure and density of states to the de-excitation of the Si (3p) electron to the Fe (3d) ground state. The DOS has helped explain why this feature has not been observed to date. By the DOS calculation, we have found that this feature comes from minority electrons. We then have shown that FeSi cannot only be used in infrared application but also can be a UV emitter.
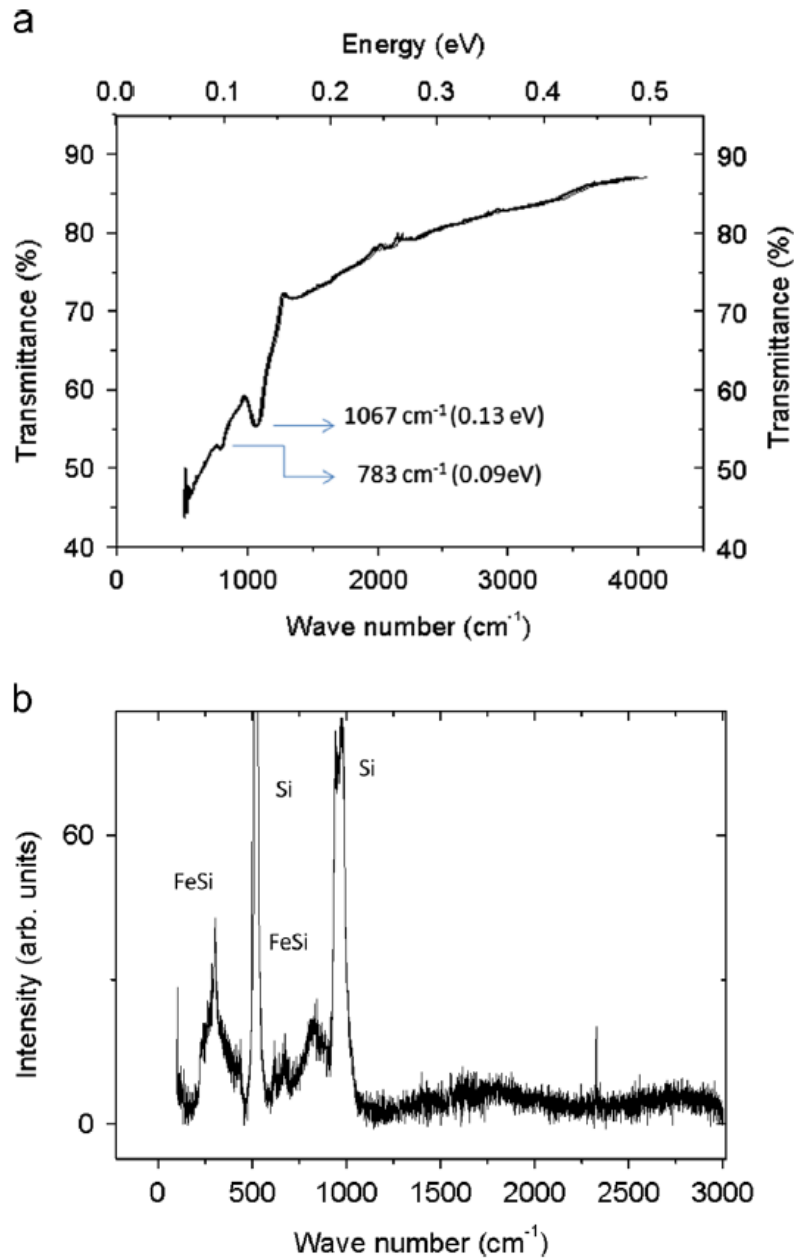
Fig. 7. (a) Typical Fourier transform infrared spectrum of c-FeSi/Si nanofibre sample showing the two major IR absorptions by TO and LO phonon at 783 cm^{-1} and 1066 cm^{-1} wave-numbers, respectively. The latter agrees perfectly with the band gap of FeSi as calculated by DFT. (b) Raman spectrum for the ε-FeSi/Si nano-fibres grown on a Si substrate.

References

[1] J.R. Szczech, S.Jin, J.Mater.Chem.20(2010)1375.

[2] S. Hung, T.T.Wang, L.Chu, L.Chen., J.Phys.Chem.C.115(2011)15592.

[3] A.L. Schmitt, M.J. Bierman, D. Schmeisser, F.J. Himpsel, S. Jin, Nano Lett. 6 (2006) 1618.

[4] S. Liang, X. Fang, T. Xia, Y. Qing, Z. Guo, J. Phys. Chem. C. 114 (2010) 16187.

[5] Y. Xia, P. Yang, Y. Sun, Y. Wu, B Mayers, B. Gates, Y. Yin, F. Kim, H. Yan, Adv. Mater. 15 (2003) 353.

[6] L. Ouyang, E.S. Thrall, M.M. Deshmukh, H. Park, Adv. Mater. 18 (2006) 1437.

[7] E. Kulatov, H. Ohta, T. Arioka, S. Halilov, L Vinokurova, J. Phys. Condens. Matter 9 (1997) 9043.

[8] S. Witanachchi, H. Weerasingha, H. Abou Mourad, P. Mukherjee, Physica B 405 (2010) 208.

[9] Z. Schlesinger, Z. Fisk, H. Zang, M.B Maple, Physica B 237-238 (1997) 460.

[10] I. Goldfarb, Surf. Sci. 554 (2004) L87.

[11] T. Koga, A Bright, T. Suzuki, K. Shimada, H Tatsuoka, H. Kuwabara, Thin Solid Films 369 (2000) 248.

[12] B.W. Mwakikunga, E. Sideras-Haddad, M. Maaza, Opt. Mater. 29 (2007) 481.

[13] B.W. Mwakikunga, A. Forbes, E. Sideras-Haddad, C. Arendse, Phys. Status Solidi A 150 (2008) 205.

[14] B.W. Mwakikunga, A. Forbes, E. Sideras-Haddad, M. Scriba, Nanoscale Res. Lett. 5 (2010) 189.

[15] L. Shikwambana, M. Govender, B.W. Mwakikunga, Adv. Mater. Res. 227 (2011) 80.

[16] F.J Morin, Phys. Rev. Lett. 3 (1959) 34.

[17] B.W Mwakikunga, A.E. Mudau, N. Brink, C.J. Willers, Appl. Phys. B 105 (2011) 451.

[18] B.W Mwakikunga, M Maaza, K.T. Hillie, C.J. Arendse, T. Malwela, E. Sideras-Haddad, 61, 105 (2012).

[19] J.P. Perdew, K. Burke, M. Ernzerhop, Phys. Rev. Lett. 77 (1990) 3865.

[20] M.C. Payne, M.P. Teter, D.C. Allan, T.A. Arias, J.D. Joannopoulos, Rev. Mod. Phys. 64 (1992) 1045.

[21] D. Vanderbilt, Phys. Rev. B: Condens. Matter 41 (1990) 7892.

[22] H.J. Monkhorst, J.D. Pack, Phys. Rev. B: Condens. Matter 13 (1976) 5188.

[23] A.L Patterson, Phys. Rev. 56 (1939) 978.

[24] G.K Williamson, W.H Hall, Acta Metall. 1 (1953) 22.

[25] B. Schuller, R. Carius, S. Lenk, S. Mantl, Opt. Mater. 17 (2001) 121.

[26] K. Yoneda, Y. Terai, K. Noda, N. Miura, Y. Fujiwara, Physics Procedia 11 (2011) 185. [27] M.Z Hossain, T. Mimura, S. Uekusa, J. Lumin. 129 (2009) 931.

[28] K. Shimura, K. Yamaguchi, M. Sasase, H. Yamamoto, S. Shamoto, K. Hojou, Vacuum 80 (2006) 719.

[29] Y. Maeda, Y. Terai, M. Itakura, N. Kuwano, Thin Solid Films 461 (2004) 160.

[30] H.T Chen, X.L Wu, Y.Y Zhang, W.N Su, App. Phys. A 97 (2009) 725.

[31]   A. Mimura, M. Fujii, S. Hayashi, K. Yamamoto, J. Lumin. 87-89 (2000) 429.

[32]   Al.L. Efros, A.L. Efros, Sov. Phys. Semicond. 16 (1982) 772.

[33]   L.F. Mattheiss, D.R. Hamann, Phys. Rev. B: Condens. Matter 47 (1993) 13114.

[34]   M.R. Beversluis, A. Bouhelier, L. Novotny, Phys. Rev. B: Condens. Matter 68 (2003) 1. [35] C.J. Arendse, G.F. Malgas, T.F.G. Muller, D. Knoesen, C.J. Oliphant, D.E. Motaung, S. Halindintwali, B.W. Mwakikunga, Nanoscale Research Letters 4 (2009) 307.